

Understanding the Effect of Lead Iodide Excess on the Performance of Methylammonium Lead Iodide Perovskite Solar Cells

Zeeshan Ahmad,[†] Rebecca A. Scheidt,[‡] Matthew P. Hautzinger,[‡] Kai Zhu,[‡]
Matthew C. Beard,[‡] and Giulia Galli^{*,†,¶,§}

[†]*Pritzker School of Molecular Engineering, University of Chicago, Chicago, Illinois 60637,
United States*

[‡]*Chemistry & Nanoscience Center, National Renewable Energy Laboratory, Golden,
Colorado 80401, United States*

[¶]*Department of Chemistry, University of Chicago, Chicago, Illinois 60637, United States*

[§]*Argonne National Laboratory, Lemont, Illinois 60439, USA*

E-mail: gagalli@uchicago.edu

Abstract

The presence of unreacted lead iodide in organic-inorganic lead halide perovskite solar cells is widely correlated with an increase in power conversion efficiency. We investigate the mechanism for this increase by identifying the role of surfaces and interfaces present between methylammonium lead iodide perovskite films and excess lead iodide. We show how type I and II band alignments arising under different conditions result in either passivation of surface defects or hole injection. Through first-principles simulations of solid-solid interfaces, we find that lead iodide captures holes from methylammonium lead iodide and modulates the formation of defects in the perovskite, affecting

recombination. Using surface-sensitive optical spectroscopy techniques, such as transient reflectance and time-resolved photoluminescence, we show how excess lead iodide affects the diffusion and surface recombination velocity of charge carriers in methylammonium lead iodide films. Our coupled experimental and theoretical results elucidate the role of excess lead iodide in perovskite solar cells.

Hybrid organic-inorganic perovskites are ideal candidates for many photovoltaic and optoelectronic applications due to their low-cost solution processability, scalable manufacturing, high absorption coefficients, and long carrier lifetimes.¹⁻⁴ Perovskite solar cells (PSC) have shown outstanding improvements at the device level over a short period of time with power conversion efficiencies exceeding 25%.⁵ The pace of understanding the microscopic origin of such high efficiency, however, has been much slower.

Recently, there has been great interest in improving the efficiency of solution-processed PSCs through the incorporation of excess PbI_2 in the precursor solution.⁶⁻¹⁰ Various studies have attempted to understand the influence of the excess PbI_2 , especially as it relates to methylammonium lead iodide (MAPI) which is widely used as a case study to make inferences about other, more complex perovskite compositions. Many of these investigations have primarily focused on the effect of PbI_2 on defect passivation to explain the increase in solar cell efficiency,^{6,11} including studies showing an increase of open-circuit potential when excess PbI_2 is added;^{12,13} other studies however observed no change upon addition of PbI_2 or even a decrease in open-circuit potential.^{6,9} Discrepancies also exist regarding the energy level alignment between MAPI and PbI_2 and its role in determining the effect of PbI_2 on PSCs. Chen et al.⁷ found type I alignment between MAPI and PbI_2 and proposed that PbI_2 increases the power conversion efficiency through passivation at grain boundaries and interfaces, thus resulting in reduced carrier recombination. However, Calloni et al.¹⁴ showed that a PbI_2 layer is formed *in situ* during annealing and sputtering at the surface of MAPI and exhibited a type II band alignment which can be used for hole extraction and thus increasing charge separation. Similarly, Roose et al.⁹ showed that excess PbI_2 forms a thin

(< 5 nm) layer at the surface of the perovskite that assists in charge extraction. Further, the MAPI crystallite size has been found to increase with excess PbI_2 in one study¹⁰ while another study found no significant effect of thickness.⁹ PbI_2 is photoactive and a source of parasitic losses, as it can absorb photons with wavelengths close to 450 nm. However spatially resolved photoluminescence indicated that the carriers generated in PbI_2 migrate to the interface with MAPI and eventually contribute to the open-circuit voltage.¹² Detrimental effects of excess PbI_2 have also been observed, namely a worsening of the stability of the PbI_2 -rich perovskite samples and the presence of a high trap density responsible for lowering the photovoltaic performance.¹⁵⁻¹⁷

The wide discrepancies found in the literature suggest that the effects of unreacted PbI_2 in PSCs are still not fully understood and are dependent not only on the amount of excess PbI_2 but also on the processing conditions. A microscopic modeling of perovskite/ PbI_2 interfaces is required to validate experimental findings^{12,18,19} and provide detailed mechanistic explanations, which in turn may be used to derive design rules for device optimization. Previous studies have mostly used device level parameters such as measured photocurrent, voltage, and fill factor to explain the enhanced performance of PSCs with excess PbI_2 . At present, a detailed understanding of the effect of charge carrier dynamics and defect formation in the presence of excess PbI_2 is still missing.

Here, using theory and experiments we perform a comprehensive investigation of the role of surfaces and interfaces present in MAPI thin films when excess PbI_2 is used in the precursor solutions. Using density functional theory (DFT) calculations, we study how various surface terminations of MAPI interfaced with PbI_2 lead to different energy level alignments and localization of the energy levels at the valence band maximum (VBM) and the conduction band minimum (CBM) of MAPI. We use our theoretical results to explain the effects of excess PbI_2 and resolve several discrepancies found in the literature. In particular, we perform semi-local and hybrid DFT calculations on various possible interfaces between MAPI and PbI_2 , and we use our results to quantify the charge extraction mechanism and formation energy

of interfacial defects. In addition, we carry out optical experiments to probe the behavior of charge carriers at the surfaces of MAPI with various amounts of PbI_2 present in the precursor solution. We find agreement between our theoretical and experimental results, leading to further clarification of the role of excess PbI_2 in PSCs. Finally, we provide design guidelines for maximizing the beneficial aspects of excess PbI_2 on the performance of PSCs.

We performed hybrid DFT calculations using the Heyd–Scuseria–Ernzerhof (HSE) functional to obtain accurate energy level alignments between MAPI and PbI_2 as a function of surface termination. For MAPI, we consider the dominant (001) and (110) surfaces²⁰ with PbI_2 and MAI terminations, while for PbI_2 , we consider the $(10\bar{1}0)$ surface with Pb and I terminations as shown in Fig. 1. The intrinsic differences in the composition and bonding at different surface terminations result in different energy level alignments. Fig. 2 shows the

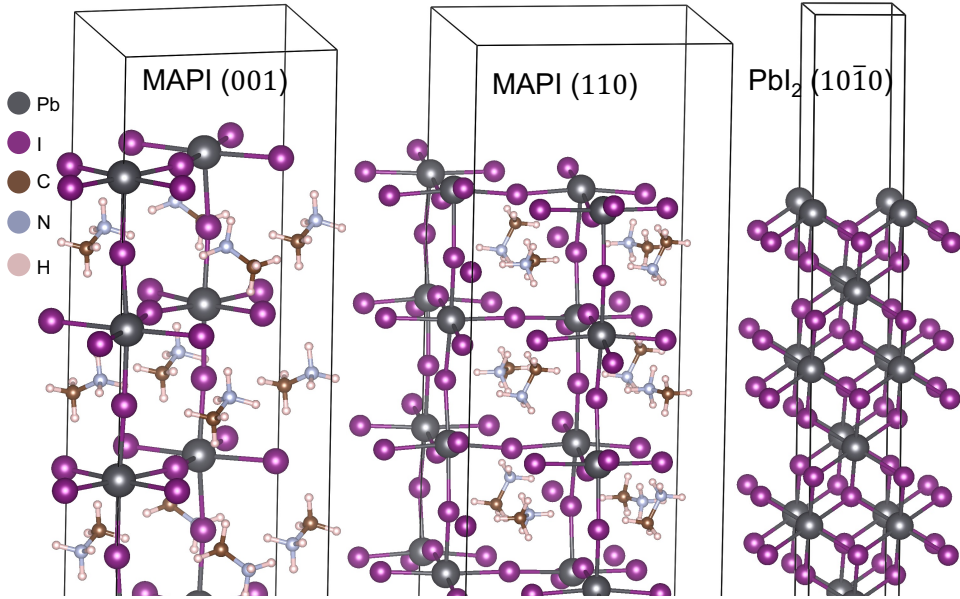


Figure 1: Ball and stick representation of the atomistic structures of the surfaces of MAPI and PbI_2 . The left and middle panels show the dominant (001) and (110) surfaces of MAPI respectively, that were used to generate an interface with $(10\bar{1}0)$ surface of PbI_2 , shown in the right panel. For MAPI, the layers show PbI_2 and MAI terminations while the PbI_2 surface could be terminated by Pb or I atoms.

energy level alignments between PbI_2 and (001) and (110) surfaces of MAPI (a and b respectively). In our notation, the species after the hyphen represents the surface termination,

for example, MAPI–PbI₂ refers to the PbI₂ surface termination of MAPI and PbI₂–I refers to the iodine terminated surface of PbI₂. First, we focus on MAPI surfaces with PbI₂ termination. We find that both (001) and (110) surfaces have a type II alignment with PbI₂, allowing hole transfer from the MAPI valence band to PbI₂ but blocking electron transfer. The energy loss of the hole on moving to the Pb terminated PbI₂ surface is larger than in the case of the I terminated surface. For MAPI surfaces with MAI termination, we obtain a type I interface for MAPI (001) interfaced with Pb terminated PbI₂ and type II with I terminated PbI₂. The type I alignment effectively blocks the transfer of electrons and holes and Pb terminated PbI₂ passivates the surface of MAPI.⁷ The type II alignment observed here, however, which is due to the CBM of PbI₂ being slightly lower in energy than that of MAPI, allows for the transfer of electrons. For the MAPI (110) surface, the alignment is of type I with I terminated and type II with Pb terminated PbI₂ surface. The raising of the VBM level of MAI terminated MAPI is consistent with the observations of Meggiolaro et al.²¹. In this case, the VBM level of MAPI is raised above the energy level of the hole transport layer resulting in blocking hole transfer.

Our computed energy level diagrams show that both type I and type II alignments may arise, depending on the terminations of MAPI and PbI₂ surfaces. As the amount of PbI₂ is increased and a higher proportion of MAPI surfaces are covered by PbI₂, a transition to a primarily type II band alignment is observed which favors hole transfer to PbI₂. Due to the type II alignment, charge carriers can be more effectively separated, resulting in reduced recombination. Additionally, in a n-i-p configuration, where the perovskite layer is placed between the electron and hole transport layers, the transfer of holes to the hole transport layer can be enhanced due to the proximity to the PbI₂ terminated surface.¹⁴

The energetics of the photogenerated electrons and holes is not only affected by the surface facet and termination of MAPI and PbI₂, but also by the interfacial strain, arising due to lattice mismatch. For example, Rothmann et al.²² imaged formamidinium lead iodide (FAPbI₃) solar cells and showed the existence of coherent interfaces between FAPbI₃ and

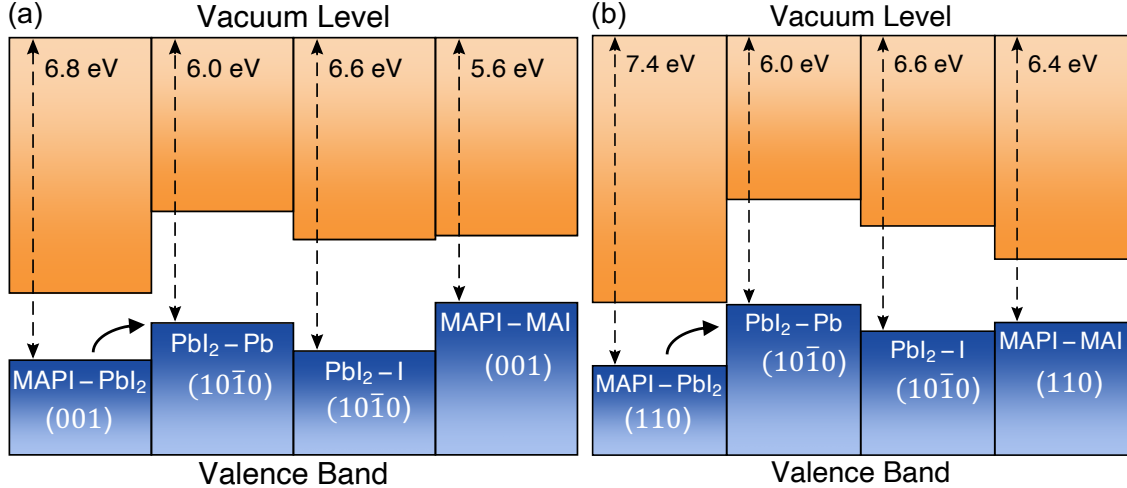


Figure 2: Energy level alignment diagram based on (a) (001) and (b) (110) surfaces of MAPI with PbI_2 ($10\bar{1}0$) surface. Both type I and type II alignments are possible depending on the facet and termination of MAPI and PbI_2 . Notably, the PbI_2 termination of MAPI always results in a type II alignment with PbI_2 , while both type I and II alignments are possible with the MAI termination. Generated using band alignment plotting tool, <https://github.com/utf/bapt>.

PbI_2 with low lattice distortion. Hence it is interesting to identify possible commensurate interfaces between MAPI and PbI_2 and study their electronic properties. We characterize the interface by the Miller indices of the surfaces of MAPI and PbI_2 in contact with each other, their termination, and individual rotations about the axis perpendicular to the interface. To accommodate the lattice mismatch, we consider several possible multiplicities of the in-plane lattice vectors of MAPI and PbI_2 that result in computationally tractable supercell sizes (Our supercells contain from 120 to 456 atoms, corresponding to 624 and 2272 valence electrons). For all interfaces, we only consider the PbI_2 termination of MAPI in contact with the Pb and I terminations of PbI_2 surfaces to study the effects of excess PbI_2 . We consider six commensurate interfaces between MAPI and PbI_2 , which span the (001) and (110) surfaces of MAPI and the ($10\bar{1}0$) surface of PbI_2 . All interfaces are listed in Table S2 in the Supplementary Information. While the strain on PbI_2 may be as large as $\sim 10\%$, we note that along the c axis (perpendicular to the interface) the strain may be easily accommodated due to the presence of interlayer van der Waals interactions. Further, the energy increase caused by strain can be easily offset by the additional bonding between the surfaces of MAPI

and PbI_2 when the PbI_2 film is only a few layers thick.⁹ The initial distance between the surfaces of MAPI and PbI_2 is set in such a way that Pb-I bonds with bond lengths similar to those found in MAPI ($\sim 3.5 \text{ \AA}$) are formed connecting the surfaces of MAPI and PbI_2 . Fig. 3 displays the positions of the VBM and CBM for the six different interfaces between MAPI and PbI_2 considered here. As shown in Figs. 3(a) and (c), we find that the holes are localized within the PbI_2 layers and near the interface, consistent with the band alignment discussed above. This localization is more prominent for the Pb termination. The CBM, as shown in Figs. 3(b) and (d), on the other hand, is localized within the bulk of MAPI. This result further confirms that the effect of excess PbI_2 is to collect the holes, resulting in charge carrier separation and efficient transfer to the hole transport layer. However, if PbI_2 turns out to be completely surrounded by MAPI, it may be detrimental to the device performance, since its presence will result in the trapping of holes that will have no clear path to the hole transport layer.

Deep traps that limit the power conversion efficiency of PSCs have been shown to concentrate mostly at the surfaces and interfaces present in polycrystalline thin films.¹⁹ The presence of interfacial defects has been proposed as the cause of the increase of photovoltage at energies below the band gap as the PbI_2 content in the PSC is increased.⁸ The critical role of surfaces and interfaces is also highlighted in studies on grain size dependence of the perovskite properties.²³⁻²⁵ For example, the $\text{I}_i^-/\text{V}_I^+$ Frenkel pair, where I_i^- represents negatively charged interstitial iodine and V_I^+ represents a positively charged iodine vacancy, is under active investigation due to its known role in voltage hysteresis and light-induced photoluminescence enhancement and in voltage decrease in MAPI solar cells.²⁶⁻²⁸ Meggiolaro et al.²⁹ showed that the formation energy of an $\text{I}_i^-/\text{V}_I^+$ Frenkel pair decreases drastically from 0.86 eV in the bulk to 0.03 eV at the PbI_2 terminated MAPI surface. This change of energy landscape can result in surface defects dominating the non-radiative recombination characteristics of MAPI PSCs. In MAPI thin films with excess PbI_2 , however, the interfaces between the two materials are expected to play a more important role in the recombination

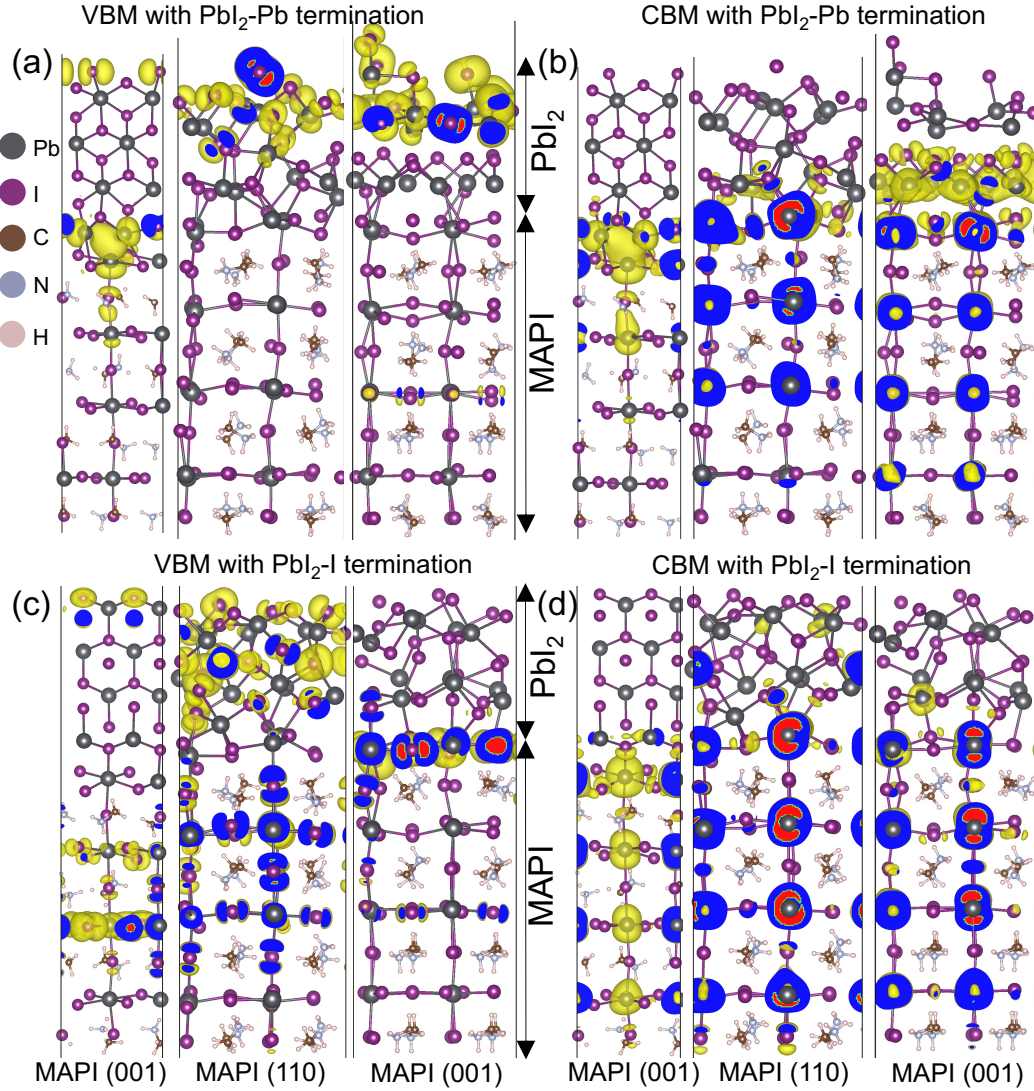


Figure 3: Positions of the valence band maximum (VBM) and conduction band minimum (CBM) for the six interfaces between MAPI and the $(10\bar{1}0)$ surface of PbI₂ considered in this study shown using isosurfaces of electron density for the respective bands. (a) and (b) show respectively the VBM and CBM positions for interfaces with Pb terminated PbI₂, while (c) and (d) show the same for interfaces with I terminated PbI₂. The blue and red colors appear at the locations of the slicing plane. The interfaces are ordered according to Table S1 and generated using three different surfaces of MAPI: (001), (110), and (001) rotated 45 degrees about the axis perpendicular to the interface. The VBM orbitals (a and c) are localized mostly within PbI₂ or at the interface while the CBM orbitals (b and d) lie within the bulk of MAPI.

of charge carriers. Admittance spectroscopy characterization of perovskite thin films revealed that PbI_2 -rich MAPI PSCs had a lower defect density which resulted in longer carrier lifetimes.¹³

Motivated by previous experimental and theoretical studies of defects, we performed DFT calculations of the $\text{I}_i^-/\text{V}_I^+$ Frenkel pair in MAPI bulk, surfaces, and interfaces between MAPI and PbI_2 . Fig. S1 shows the structure of MAPI containing this defect with the I terminated PbI_2 layer on top. Table 1 compares the formation energy of the $\text{I}_i^-/\text{V}_I^+$ Frenkel pair in MAPI at bulk, surfaces, and interfaces calculated using the Perdew–Burke–Ernzerhof (PBE) functional without spin-orbit coupling (SOC) and the HSE functional with SOC (following common practice in functional comparisons for perovskites, due to cancellation of errors arising from the semi-local functional and spin-orbit effects³⁰). As expected, the defect formation energy in MAPI decreases from 1.16 eV for the bulk to 0.21 eV for (001) surface and is approximately zero for the (110) surface. The defect formation energies for the bulk and (001) surface agree well with a previous first-principles investigation.²⁹ The defect formation energy for the MAPI (110) surface obtained with the HSE functional is close to zero (it is in fact slightly negative, -0.01 eV, possibly due to the fact that the HSE calculation was performed for PBE-optimized geometries), implying that the (110) surface might harbor a high density of defects. The defect formation energies of MAPI/ PbI_2 interfaces follow two different trends depending on the surface termination of PbI_2 in contact with MAPI. With Pb terminated PbI_2 , the defect formation energy is increased compared to that of the bare MAPI surface. The defect formation energies of the I terminated surfaces, on the other hand, are comparable to those of the bare MAPI surfaces (both (001) and (110) surfaces); hence we conclude that a I-rich PbI_2 might not provide the beneficial effect of lowering the trap density. Another benefit of using PbI_2 in I-poor conditions is that the formation of I interstitials in MAPI, that act as deep traps, is inhibited in these conditions. Iodine vacancies, on the other hand, that are formed under I-poor conditions create only shallow traps as shown by hybrid DFT calculations.^{30,31}

Table 1: The formation energy of the I_i^-/V_i^+ Frenkel pair in MAPI at bulk, surfaces, and interfaces. The formation energy decreases considerably at the PbI_2 terminated surfaces, compared to the value in the bulk of MAPI. An interface of MAPI with PbI_2 decreases the defect density under I-poor conditions but increases it under I-rich conditions.

Structure		Defect Formation Energy	
		PBE (eV)	HSE+SOC (eV)
Bulk MAPI		1.12	1.16
MAPI (001) surface		0.03	0.21
MAPI (110) surface		0.12	~ 0 .
Interfaces			
MAPI surface	PbI_2 surface		
(100)	(10 $\bar{1}$ 0)-Pb	0.90	1.08
(110)	(10 $\bar{1}$ 0)-Pb	0.63	0.54
(100)	(10 $\bar{1}$ 0)-I	0.18	0.10
(110)	(10 $\bar{1}$ 0)-I	0.04	0.03

We now turn to experiments to validate our theoretical predictions on energy level alignment, charge extraction, and defect formation energies. The type of band alignment present at MAPI and PbI_2 interfaces influences the surface recombination and charge carrier diffusion at the perovskite interface and we explore these effects by carrying out optical measurements.

Several experimental studies have attempted to show how excess PbI_2 affects the performance of MAPI PSCs. Few studies, however, probe the effects on charge carrier dynamics at the surface of the film, where the interaction between MAPI and PbI_2 is the most notable. Using a suite of optical characterization methods, we elucidate the behavior of charge carriers at the surface of polycrystalline MAPI thin films with excess amounts of PbI_2 ranging from 0% (stoichiometric) to 10% excess, corresponding to typical values considered in the literature. By combining ultrafast transient reflectance (TR) spectroscopy with time-resolved photoluminescence (TRPL), we determined the diffusion coefficient and surface recombination velocity (SRV) of carriers in MAPI films.

Ultrafast TR spectroscopy, which utilizes an above band gap excitation pump pulse and broadband, white-light probe pulse centered around the band edge, can probe carrier dynamics at various film depths on a picosecond to nanosecond regime.^{32,33} By varying the pump energy (i.e. the wavelength of light used in the excitation pulse) different volumes of the

sample of interest can be studied due to changes in the absorption coefficient of the material of interest. At high pump photon energies (and correspondingly shallow pump penetration depths), charge carrier dynamics can primarily be attributed to diffusion of charge carriers away from the surface of the sample, since the probe is only sensitive to within about 10 nms of the surface of the material. However, low- photon pump energies are able to penetrate much farther into the sample film, such that the probed charge carrier behavior is more akin to bulk behavior seen in traditional transient absorption (TA) spectroscopy (Figs. S2 and S3). The recombination dynamics of low photon energy TR (and by extension TA) reflected both the bulk recombination and surface recombination. Therefore, differences in the TR dynamics taken with different pump excitation wavelengths can be attributed to the SRV since the bulk lifetime remains the same for the material. By using various pump photon energies, a correlation between the carrier dynamics taken with different excitation energies can be used in a global fit analysis to extract the SRV as well as the diffusion coefficient. Capturing the SRV of carriers in defect tolerant metal halide perovskites using TR, however, can be challenging due to their low surface recombination rates.³⁴ The low SRV of carriers in these systems results in recombination lifetimes larger than the maximum time scale of 2.5 ns analyzed using our TR instrument.³⁵ Therefore, we use TRPL to deconvolve the carriers' SRV from bulk recombination processes by following the recombination lifetime of the carriers as a function of sample thickness for each stoichiometry of interest. The SRV is calculated by plotting the PL lifetime τ_{PL} as a function of film thickness L (Fig. S4) and using the relation $1/\tau_{\text{PL}} = \text{SRV}/L + 1/\tau_{\text{bulk}}$ where τ_{bulk} is the bulk lifetime. Thus, by coupling the two techniques of TR and TRPL, we can extract both the diffusion coefficient and SRV of photo-carriers, respectively, for MAPI films with 0, 2.5, 5, and 10% excess PbI_2 .

The diffusion coefficient and SRV are shown in Fig. 4. The diffusion coefficient increases with increasing amounts of PbI_2 , with 10% excess showing the highest diffusion coefficient of photogenerated charge carriers. At 5% excess PbI_2 , there is a drop in the diffusion coefficient with a value close to that for the stoichiometric sample. The overall trend observed for

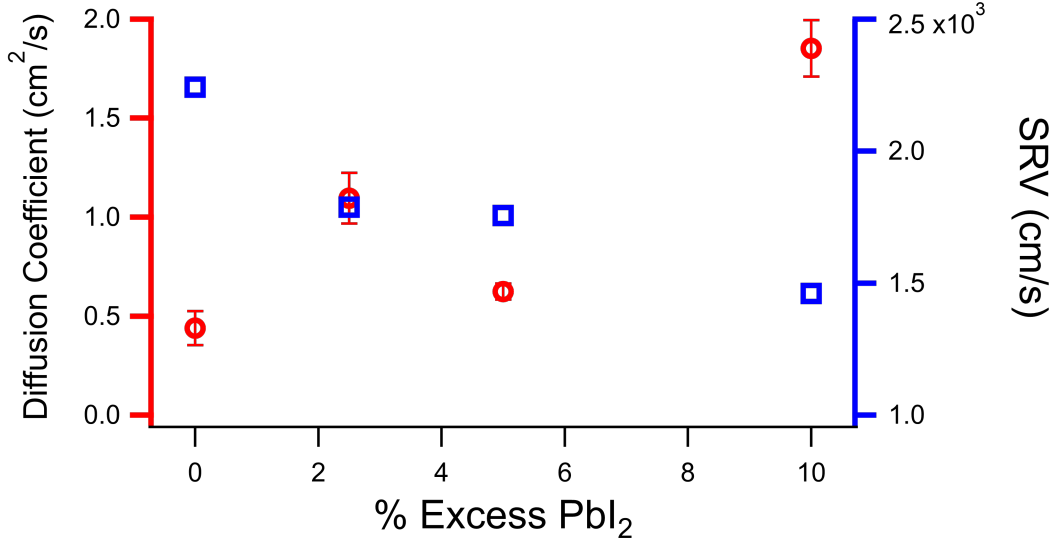


Figure 4: The diffusion coefficient (red, left axis) and the surface recombination velocity (SRV) (blue, right axis) as a function of excess PbI₂ in the MAPI films. The diffusion coefficient is obtained from the global fit analysis performed on the transient reflectance data (Fig. S3). Increasing amounts of PbI₂ yields increasing diffusion coefficients, indicating that fewer bulk defects are present. However, in the case of 5% excess PbI₂, the diffusion coefficient is similar to the stoichiometric instance. The SRV decreases with increasing amounts of PbI₂, indicating surface passivation.

the diffusion coefficient and SRV indicates that increasing the amount of PbI₂ leads to better charge carrier and lower SRV which in turn should translate to an enhanced solar cell performance. Indeed, multiple studies show that excess PbI₂ leads to better device performance, with a peak performance around 10% excess PbI₂.^{9,12,36} It was previously suggested that the presence of excess PbI₂ boosted device performance purely by passivating surface trap states created by halide ion vacancies.⁶ Since the diffusion coefficient is a measure of the ability of charge carriers to diffuse away from the surface of the film towards the bulk, this trend indicates that excess PbI₂ does not just influence the surface of MAPI films. Our results show that excess PbI₂ increases charge carrier diffusion away from the surface, as well. This may be due to faster transport (fewer defects) at grain boundaries and/or a lower number of grain boundaries in the excess PbI₂ samples, as has been proposed.⁶ However, it is important to note that the samples with different stoichiometries investigated here have similar grain sizes (Fig. S5); therefore any change in charge carrier behavior can be attributed

to other phenomena besides carrier recombination at grain boundaries. The reduced defect density at Pb terminated PbI_2 interface with MAPI predicted by theory and shown in Fig. 3, may additionally contribute to higher diffusion of charge carriers. Additionally, for all stoichiometries studied, the τ_{bulk} of the materials are the same, indicating that the changes to the PL lifetime of the samples is due solely to change in the surface recombination. This observation provides further support that excess PbI_2 affects the surface of the perovskite, and therefore the interface between the perovskite and PbI_2 .

The SRV is the propensity of charge carriers to recombine at the surface, with larger values indicating a large probability of recombination due to a higher density of recombination centers.³³ At 0% excess PbI_2 , the SRV is 2.24×10^3 m/s and it drops across the other stoichiometries down to 1.46×10^3 cm/s for the 10% excess sample. This clear trend indicates that films with excess PbI_2 have fewer defects and recombination centers at the surface than films with stoichiometric amounts of PbI_2 . The lower SRV can be due to the interplay of a combination of factors. One source of the drop in SRV can be the passivation of dangling bonds at surfaces of MAPI and changes in the defect densities at surfaces and interfaces.³³ Additionally, excess PbI_2 can act as a hole sink, creating a barrier for holes to reach the surface of the perovskite. This energy barrier is quantified by the difference in energy levels of the VBM between Pb terminated PbI_2 and MAPI shown in Fig. 2. When the holes quickly diffuse to excess PbI_2 but the electrons remain within the perovskite, reduced recombination and larger charge carrier lifetimes are expected, which is reflected in the change in SRV. It is interesting to note that while the diffusion coefficient of the 5% excess PbI_2 sample is close to that of the stoichiometric sample, the SRV is much lower. Again, while we cannot distinguish a single cause of the drop in diffusion coefficient from 2.5% to 5% excess PbI_2 , we can identify several important factors leading to such drop. First, the holes from MAPI may get trapped and immobilized within PbI_2 ; hence they do not diffuse throughout the perovskite to recombine with electrons. Such a situation may occur, for example, when pockets of PbI_2 are completely surrounded by MAPI.⁹ The drop in the diffusion coefficient may also stem

from the increased concentration of Frenkel pairs in MAPI due to the preferred formation of MAPI interfaces with I terminated PbI_2 , when the excess amount is increased from 2.5% to 5%. Our theoretical results presented earlier indicate that for I terminated surfaces, Frenkel defects can form more easily than with other terminations. The I_i^- interstitial from these Frenkel defects generated at the interface can easily migrate to the bulk of MAPI due to the low migration barrier of ~ 0.1 eV²⁹ and act as an effective hole trap within the bulk,³⁷ thereby reducing the diffusion coefficient while not affecting the SRV. However, between 5% and 10% excess, we posit that Pb terminations become more frequent than I terminations, allowing for charge extraction into the PbI_2 layer. This can be seen through the drop in SRV since charge transfer becomes more prominent than recombination. This shift towards more charge transfer than recombination is also seen in the band alignment at the interface, as predicted by theory and shown in Fig. 2.

In summary, by combining optical spectroscopy measurements with first-principles electronic structure calculations of the interfaces between MAPI and PbI_2 , we provided microscopic insights into the role of excess PbI_2 in PSCs. Consistent with previous investigations, our results point at the key role of surface terminations and interfaces in determining the properties of hybrid perovskites.^{38,39} We found that excess PbI_2 on MAPI does not just provide passivation of the MAPI surface. Depending on whether the metal or the halide terminate the PbI_2 surface, different band alignments with the MAPI are possible and, importantly, different concentrations of Frenkel defects may be present, which in turn affect the electronic structure of the interface. Our findings illustrate the important interplay between Frenkel defect formation and the microscopic structure of excess PbI_2 , especially its surface terminations, in determining the enhancement or decrease of the photoluminescence intensity of photo-excited MAPI.⁴⁰ We conclude that while excess PbI_2 provides a facile route to passivating MAPI, further enhancement of device performance would be better realized through the addition of other Pb-containing additives. For example, the addition of PbSO_4 ⁴¹ could passivate the MAPI surface with Pb terminated surfaces of the excess layer

without the detrimental effects that additional I_2 would cause. While we recognize that perovskite thin films are extremely sensitive to processing conditions,⁴² our work points at an important, general design guideline to improve device efficiency. We show that the effect of PbI_2 on device performance is not monomodal, and that PbI_2 is not an ideal additive for MAPI based devices. We recommend that other additives be explored to enhance PSC performance, specifically, ones that allow for the benefits of Pb terminations such as reduced trap densities without the detrimental effects of excess I_2 .

Acknowledgement

We thank Dr. Volker Blum for helpful discussions. The study is supported as part of the Center for Hybrid Organic Inorganic Semiconductor for Energy (CHOISE), an Energy Frontier Research Center funded by the Office of Basic Energy Sciences, Office of Science within the U.S. Department of Energy. This work was authored in part by the Alliance for Sustainable Energy, LLC, the manager and operator of the National Renewable Energy Laboratory for DOE under contract number DE-AC36-08GO28308. The views expressed in the Article do not necessarily represent the views of the DOE or the U.S. Government. The U.S. Government retains and the publisher, by accepting the article for publication, acknowledges that the U.S. Government retains a nonexclusive, paid-up, irrevocable, worldwide license to publish or reproduce the published form of this work, or allow others to do so, for U.S. Government purposes. We acknowledge the National Energy Research Scientific Computing Center (NERSC), a U.S. Department of Energy Office of Science User Facility located at Lawrence Berkeley National Laboratory, operated under Contract No. DE-AC02-05CH11231 and the Bridges-2 system supported by NSF grant number ACI-1445606 which is a part of Extreme Science and Engineering Discovery Environment (XSEDE), funded by NSF grant number ACI-1548562 for computational resources.

Supporting Information Available

Details of computational and experimental methods and a compilation of all interfaces considered in this work.

References

- (1) Green, M. A.; Ho-Baillie, A.; Snaith, H. J. The emergence of perovskite solar cells. *Nat. Photonics* **2014**, *8*, 506–514.
- (2) Huang, J.; Yuan, Y.; Shao, Y.; Yan, Y. Understanding the Physical Properties of Hybrid Perovskites for Photovoltaic Applications. *Nat. Rev. Mater.* **2017**, *2*, 17042.
- (3) Yoo, J. J.; Seo, G.; Chua, M. R.; Park, T. G.; Lu, Y.; Rotermund, F.; Kim, Y.-K.; Moon, C. S.; Jeon, N. J.; Correa-Baena, J.-P.; Bulović, V.; Shin, S. S.; Bawendi, M. G.; Seo, J. Efficient Perovskite Solar Cells via Improved Carrier Management. *Nature* **2021**, *590*, 587–593.
- (4) Li, W.; Wang, Z.; Deschler, F.; Gao, S.; Friend, R. H.; Cheetham, A. K. Chemically Diverse and Multifunctional Hybrid Organic–Inorganic Perovskites. *Nat. Rev. Mater.* **2017**, *2*, 16099.
- (5) National Renewable Energy Laboratory, Golden, Colorado, Best Research-Cell Efficiency Chart. *NREL* **2021**,
- (6) Jacobsson, T. J.; Correa-Baena, J.-P.; Anaraki, E. H.; Philippe, B.; Stranks, S. D.; Bouduban, M. E. F.; Tress, W.; Schenk, K.; Moser, J.-E. Unreacted PbI₂ as a Double-Edged Sword for Enhancing the Performance of Perovskite Solar Cells. *J. Am. Chem. Soc.* **2016**, *138*, 13.
- (7) Chen, Q.; Zhou, H.; Song, T.-B.; Luo, S.; Hong, Z.; Duan, H.-S.; Dou, L.; Liu, Y.;

- Yang, Y. Controllable Self-Induced Passivation of Hybrid Lead Iodide Perovskites toward High Performance Solar Cells. *Nano Lett.* **2014**, *14*, 4158–4163.
- (8) Supasai, T.; Rujisamphan, N.; Ullrich, K.; Chemseddine, A.; Dittrich, T. Formation of a Passivating CH₃NH₃PbI₃/PbI₂ Interface during Moderate Heating of CH₃NH₃PbI₃ Layers. *Appl. Phys. Lett.* **2013**, *103*, 183906.
- (9) Roose, B.; Dey, K.; Chiang, Y.-H.; Friend, R. H.; Stranks, S. D. Critical Assessment of the Use of Excess Lead Iodide in Lead Halide Perovskite Solar Cells. *J. Phys. Chem. Lett.* **2020**, *11*, 6505–6512.
- (10) Roldán-Carmona, C.; Gratia, P.; Zimmermann, I.; Grancini, G.; Gao, P.; Graetzel, M.; Nazeeruddin, M. K. High Efficiency Methylammonium Lead Triiodide Perovskite Solar Cells: The Relevance of Non-Stoichiometric Precursors. *Energy Environ. Sci.* **2015**, *8*, 3550–3556.
- (11) Barbé, J.; Newman, M.; Lilliu, S.; Kumar, V.; Lee, H. K. H.; Charbonneau, C.; Rodenburg, C.; Lidzey, D.; Tsoi, W. C. Localized Effect of PbI₂ Excess in Perovskite Solar Cells Probed by High-Resolution Chemical–Optoelectronic Mapping. *J. Mater. Chem. A* **2018**, *6*, 23010–23018.
- (12) Merdasa, A.; Kiligaridis, A.; Rehermann, C.; Abdi-Jalebi, M.; Stöber, J.; Louis, B.; Gerhard, M.; Stranks, S. D.; Unger, E. L.; Scheblykin, I. G. Impact of Excess Lead Iodide on the Recombination Kinetics in Metal Halide Perovskites. *ACS Energy Lett.* **2019**, *4*, 1370–1378.
- (13) Jiang, M.; Wu, Y.; Zhou, Y.; Wang, Z. Observation of Lower Defect Density Brought by Excess PbI₂ in CH₃NH₃PbI₃ Solar Cells. *AIP Adv.* **2019**, *9*, 085301.
- (14) Calloni, A.; Abate, A.; Bussetti, G.; Berti, G.; Yivlialin, R.; Ciccacci, F.; Duò, L. Stability of Organic Cations in Solution-Processed CH₃NH₃PbI₃ Perovskites: Formation of Modified Surface Layers. *J. Phys. Chem. C* **2015**, *119*, 21329–21335.

- (15) Gujar, T. P.; Unger, T.; Schönleber, A.; Fried, M.; Panzer, F.; van Smaalen, S.; Köhler, A.; Thelakkat, M. The Role of PbI_2 in $\text{CH}_3\text{NH}_3\text{PbI}_3$ Perovskite Stability, Solar Cell Parameters and Device Degradation. *Phys. Chem. Chem. Phys.* **2018**, *20*, 605–614.
- (16) Wang, H.-Y.; Hao, M.-Y.; Han, J.; Yu, M.; Qin, Y.; Zhang, P.; Guo, Z.-X.; Ai, X.-C.; Zhang, J.-P. Adverse Effects of Excess Residual PbI_2 on Photovoltaic Performance, Charge Separation, and Trap-State Properties in Mesoporous Structured Perovskite Solar Cells. *Chem. - Eur. J.* **2017**, *23*, 3986–3992.
- (17) Liu, F. et al. Is Excess PbI_2 Beneficial for Perovskite Solar Cell Performance? *Adv. Energy Mater.* **2016**, *6*, 1502206.
- (18) J. Dahlman, C.; J. Kubicki, D.; Manjunatha Reddy, G. N. Interfaces in Metal Halide Perovskites Probed by Solid-State NMR Spectroscopy. *J. Mater. Chem.A* **2021**,
- (19) Ni, Z.; Bao, C.; Liu, Y.; Jiang, Q.; Wu, W.-Q.; Chen, S.; Dai, X.; Chen, B.; Hartweg, B.; Yu, Z.; Holman, Z.; Huang, J. Resolving Spatial and Energetic Distributions of Trap States in Metal Halide Perovskite Solar Cells. *Science* **2020**, *367*, 1352–1358.
- (20) Haruyama, J.; Sodeyama, K.; Han, L.; Tateyama, Y. Termination Dependence of Tetragonal $\text{CH}_3\text{NH}_3\text{PbI}_3$ Surfaces for Perovskite Solar Cells. *J. Phys. Chem. Lett.* **2014**, *5*, 2903–2909.
- (21) Meggiolaro, D.; Mosconi, E.; Proppe, A. H.; Quintero-Bermudez, R.; Kelley, S. O.; Sargent, E. H.; De Angelis, F. Energy Level Tuning at the MAPbI_3 Perovskite/Contact Interface Using Chemical Treatment. *ACS Energy Lett.* **2019**, *4*, 2181–2184.
- (22) Rothmann, M. U.; Kim, J. S.; Borchert, J.; Lohmann, K. B.; O’Leary, C. M.; Sheader, A. A.; Clark, L.; Snaith, H. J.; Johnston, M. B.; Nellist, P. D.; Herz, L. M. Atomic-Scale Microstructure of Metal Halide Perovskite. *Science* **2020**, *370*.

- (23) Kim, H. D.; Ohkita, H.; Benten, H.; Ito, S. Photovoltaic Performance of Perovskite Solar Cells with Different Grain Sizes. *Adv. Mater.* **2016**, *28*, 917–922.
- (24) Xing, J.; Wang, Q.; Dong, Q.; Yuan, Y.; Fang, Y.; Huang, J. Ultrafast Ion Migration in Hybrid Perovskite Polycrystalline Thin Films under Light and Suppression in Single Crystals. *Phys. Chem. Chem. Phys.* **2016**, *18*, 30484–30490.
- (25) Ren, X.; Yang, Z.; Yang, D.; Zhang, X.; Cui, D.; Liu, Y.; Wei, Q.; Fan, H.; Liu, S. F. Modulating Crystal Grain Size and Optoelectronic Properties of Perovskite Films for Solar Cells by Reaction Temperature. *Nanoscale* **2016**, *8*, 3816–3822.
- (26) Azpiroz, J. M.; Mosconi, E.; Bisquert, J.; Angelis, F. D. Defect migration in methylammonium lead iodide and its role in perovskite solar cell operation. *Energy Environ. Sci.* **2015**, *8*, 2118–2127.
- (27) Eames, C.; Frost, J. M.; Barnes, P. R. F.; O’Regan, B. C.; Walsh, A.; Islam, M. S. Ionic Transport in Hybrid Lead Iodide Perovskite Solar Cells. *Nat. Commun.* **2015**, *6*, 7497.
- (28) Mosconi, E.; Meggiolaro, D.; Snaith, H. J.; Stranks, S. D.; Angelis, F. D. Light-Induced Annihilation of Frenkel Defects in Organo-Lead Halide Perovskites. *Energy Environ. Sci.* **2016**, *9*, 3180–3187.
- (29) Meggiolaro, D.; Mosconi, E.; De Angelis, F. Formation of Surface Defects Dominates Ion Migration in Lead-Halide Perovskites. *ACS Energy Lett.* **2019**, *4*, 779–785.
- (30) Du, M.-H. Density Functional Calculations of Native Defects in CH₃NH₃PbI₃: Effects of Spin–Orbit Coupling and Self-Interaction Error. *J. Phys. Chem. Lett.* **2015**, *6*, 1461–1466.
- (31) Meggiolaro, D.; Motti, S. G.; Mosconi, E.; Barker, A. J.; Ball, J.; Perini, C. A. R.;

- Deschler, F.; Petrozza, A.; Angelis, F. D. Iodine Chemistry Determines the Defect Tolerance of Lead-Halide Perovskites. *Energy Environ. Sci.* **2018**, *11*, 702–713.
- (32) Chen, X.; Wang, K.; Beard, M. C. Ultrafast probes at the interfaces of solar energy conversion materials. *Phys. Chem. Chem. Phys.* **2019**, *21*, 16399–16407.
- (33) Yang, Y.; Yang, M.; Moore, D. T.; Miller, E. M.; Zhu, K.; Beard, M. C. Top and bottom surfaces limit carrier lifetime in lead iodide perovskite films. *Nat. Energy* **2017**, *2*, 16207.
- (34) Stranks, S. D.; Eperon, G. E.; Grancini, G.; Menelaou, C.; Alcocer, M. J. P.; Leijtens, T.; Herz, L. M.; Petrozza, A.; Snaith, H. J. Electron-Hole Diffusion Lengths Exceeding 1 Micrometer in an Organometal Trihalide Perovskite Absorber. *Science* **2013**, *342*, 341–344.
- (35) Zhai, Y.; Wang, K.; Zhang, F.; Xiao, C.; Rose, A. H.; Zhu, K.; Beard, M. C. Individual Electron and Hole Mobilities in Lead-Halide Perovskites Revealed by Noncontact Methods. *ACS Energy Lett.* **2020**, *5*, 47–55.
- (36) Shi, B.; Yao, X.; Hou, F.; Guo, S.; Li, Y.; Wei, C.; Ding, Y.; Li, Y.; Zhao, Y.; Zhang, X. Unraveling the Passivation Process of PbI₂ to Enhance the Efficiency of Planar Perovskite Solar Cells. *J. Phys. Chem. C* **2018**, *122*, 21269–21276.
- (37) Zhang, X.; Turiansky, M. E.; Shen, J.-X.; Van de Walle, C. G. Iodine Interstitials as a Cause of Nonradiative Recombination in Hybrid Perovskites. *Phys. Rev. B* **2020**, *101*, 140101.
- (38) Huang, Z.; Vardeny, S. R.; Wang, T.; Ahmad, Z.; Chanana, A.; Vetter, E.; Yang, S.; Liu, X.; Galli, G.; Amassian, A.; Vardeny, Z. V.; Sun, D. Observation of Spatially Resolved Rashba States on the Surface of CH₃NH₃PbBr₃ Single Crystals. *Appl. Phys. Rev.* **2021**, *8*, 031408.

- (39) Myung, C. W.; Javaid, S.; Kim, K. S.; Lee, G. Rashba–Dresselhaus Effect in Inorganic/Organic Lead Iodide Perovskite Interfaces. *ACS Energy Lett.* **2018**, *3*, 1294–1300.
- (40) Motti, S. G.; Meggiolaro, D.; Barker, A. J.; Mosconi, E.; Perini, C. A. R.; Ball, J. M.; Gandini, M.; Kim, M.; De Angelis, F.; Petrozza, A. Controlling Competing Photochemical Reactions Stabilizes Perovskite Solar Cells. *Nat. Photonics* **2019**, *13*, 532–539.
- (41) Yang, S.; Chen, S.; Mosconi, E.; Fang, Y.; Xiao, X.; Wang, C.; Zhou, Y.; Yu, Z.; Zhao, J.; Gao, Y.; Angelis, F. D.; Huang, J. Stabilizing Halide Perovskite Surfaces for Solar Cell Operation with Wide-Bandgap Lead Oxysalts. *Science* **2019**, *365*, 473–478.
- (42) Herz, L. M. Charge-Carrier Mobilities in Metal Halide Perovskites: Fundamental Mechanisms and Limits. *ACS Energy Lett.* **2017**, *2*, 1539–1548.

Supporting Information:
Understanding the Effect of Lead Iodide
Excess on the Performance of
Methylammonium Lead Iodide Perovskite
Solar Cells

Zeeshan Ahmad,[†] Rebecca A. Scheidt,[‡] Matthew P. Hautzinger,[‡] Kai Zhu,[‡]
Matthew C. Beard,[‡] and Giulia Galli^{*,†,¶,§}

[†]*Pritzker School of Molecular Engineering, University of Chicago, Chicago, Illinois 60637,
United States*

[‡]*Chemistry & Nanoscience Center, National Renewable Energy Laboratory, Golden,
Colorado 80401, United States*

[¶]*Department of Chemistry, University of Chicago, Chicago, Illinois 60637, United States*

[§]*Argonne National Laboratory, Lemont, Illinois 60439, USA*

E-mail: gagalli@uchicago.edu

Computational Details

All DFT calculations have been performed using the plane wave code Quantum Espresso.^{1,2} The Perdew–Burke–Ernzerhof (PBE) exchange–correlation functional³ without spin-orbit coupling was used for geometry optimizations. On the relaxed structures, single point DFT calculations using the Heyd–Scuseria–Ernzerhof (HSE) hybrid functional⁴ with spin-orbit coupling were performed. The DFT-D3 scheme proposed by Grimme was used to account for the van der Waals dispersion.⁵ For PBE calculations, we used the ultrasoft GBRV pseudopotentials with the suggested energy cutoffs of 40 Ry for the wavefunction and 320 Ry for the density.⁶ For the HSE calculations, we used SG15 ONCV pseudopotentials⁷ with a 70 Ry energy cutoff for the wavefunction, 280 Ry for the density, and 70 Ry for the exact exchange operator. For interfacial calculations, we used I pseudopotential with 7 valence electrons instead of 17 to reduce the computational cost. The fraction of the exact exchange used for both MAPI and PbI_2 was 0.43 which has been shown to provide a better agreement with the experimental band gap of MAPI.⁸ For PbI_2 as well, the band gap using this value of exact exchange is in agreement with experiment as shown in Table S1.⁹ For surfaces and interfaces, the periodic images were separated by 15 Å of vacuum for PBE calculations and 10 Å for the HSE calculations to save memory. HSE calculations performed using 15 Å vacuum showed negligible change in the energies. The pymatgen¹⁰ and atomic simulation environments¹¹ were used for generating surface and interfacial structures while the visualization was done using the VESTA package.¹² For defect formation energy calculations using HSE functional, reduced energy cutoffs of 40 Ry for the wavefunction and 80 Ry for the exact exchange operator were used which have been shown to agree well with those calculated at 70 Ry energy cutoffs due to error cancellation for the pristine and defective structures.¹³ For MAPI, we

Table S1: Band gaps obtained using hybrid functional with fraction of exact exchange = 0.43.

Material	Band gap (eV)
MAPI	1.42
PbI_2	2.36

used the experimental lattice constants 8.849 Å and 12.642 Å .¹⁴ For PbI₂, the structure # 9009114¹⁵ from crystallography open database¹⁶ with spacegroup P $\bar{3}$ m1 was used. The ionic positions are relaxed according to convergence criteria of at most 0.001 Ry/Bohr for forces and 0.0001 Ry for energies. For some pristine structures, reduced force convergence criteria had to be used to obtain the defect formation energies due to the shallow nature of the energy landscape. An example of an interfacial defect is shown in Fig. S1

The interfaces identified are shown in Table S2 have in plane lattice vectors normal to each other. This enforces the PbI₂ surface to be (10 $\bar{1}$ 0) with its lattice vectors b and c in the plane of the interface.

Table S2: Possible interfaces between different surfaces of MAPI and PbI_2 . All interfaces studied use the PbI_2 termination of MAPI in order to study PbI_2 excess effects. The table shows the surface facets of MAPI and PbI_2 , the in plane lattice vectors a_1 and a_2 and strains in those directions. For interfaces besides those with MAPI (001) in rows 1 and 2, we fixed the in-plane lattice vectors to the MAPI values since the existence of small amounts of PbI_2 is not expected to influence MAPI axes considerably.

MAPI (001) with Pb terminated PbI_2 ($10\bar{1}0$), with cell relaxation					
Lattice vector	MAPI	PbI_2	Interface	strain MAPI (%)	strain PbI_2 (%)
a_1	a=8.849	2a=9.11	9.06	2.33	-0.60
a_2	a=8.849	c=6.977	8.38	-5.33	20.07
MAPI (001) with I terminated PbI_2 ($10\bar{1}0$), with cell relaxation					
a_1	a=8.849	2a=9.11	9.070	2.50	-0.44
a_2	a=8.849	c=6.977	8.358	-5.54	19.80
MAPI (110) with PbI_2 ($10\bar{1}0$)					
Lattice vectors fixed to MAPI values; two Interfaces: Pb and I terminations of PbI_2					
a_1	c=12.642	3b=13.665	12.642	0	-7.49
a_2	$\sqrt{2}a=12.514$	2c=13.954	12.514	0	-10.32
MAPI (001) rotated 45 degrees about [001] axis with PbI_2 ($10\bar{1}0$)					
Lattice vectors fixed to MAPI values; two Interfaces: Pb and I terminations of PbI_2					
a_1	$\sqrt{2}b=12.514$	3b=13.665	12.514	0	-8.42
a_2	$\sqrt{2}a=12.514$	2c=13.954	12.514	0	-10.32

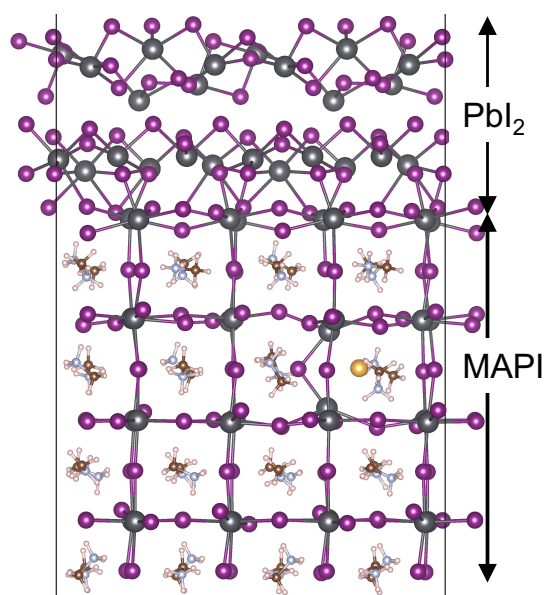


Figure S1: An I^-/V_1^+ Frenkel pair in MAPI located close to the interface with PbI_2 . The interstitial I is shown in yellow and the vacancy is located in the layer above it. The interface is of the last type mentioned in the table i.e., MAPI (001) rotated 45 degrees about $[001]$ axis with $PbI_2 (10\bar{1}0)$

Experimental Details

Sample preparation:

MAPI films were prepared according to previous reports.¹⁷ 0.5 x 1 cm quartz substrates were prepared by sonicating in isopropyl alcohol followed by sonicating in acetone. The quartz slides were ozone cleaned for 15 minutes immediately before perovskite deposition. MAPI precursor solutions were made by dissolving MAI (Dyesol) and PbI_2 (Alfa Aesar, 99.9985%, metal basis, power) in a 9:1 N,N-dimethylformamide (DMF, Sigma Aldrich, anhydrous, 99.8%):dimethylsulfoxide (DMSO, Sigma Aldrich, anhydrous, >99.9%) solution. For the stoichiometric films (0% excess PbI_2), 1.5 M films were made. To create films of other stoichiometric values, 2.5%, 5%, and 10% excess PbI_2 by molarity was added. These films were used for TR, TRPL, and XRD measurements.

Additional films for TRPL measurements were made with 0.75 and 0.375 M solutions. All solutions were prepared in a glovebox. Films were deposited using an antisolvent spin-coating method. 50 μL of the perovskite precursor solution was statically drop cast onto the films. The films were then spun at 4000 rpms for 25 seconds, with 60 μL of chlorobenzene (Sigma Aldrich, anhydrous, >99.8%) dynamically spun cast onto the film after 10 seconds of spin coating. The films were annealed for 1 minute at 65 C followed by 2 minutes at 100 C. Films were kept in a nitrogen flow box after deposition to ensure the films did not degrade under ambient conditions.

Transient reflectance measurements:

Transient reflectance measurements were performed on a Coherent Laser (800 nm fundamental beam, 1 kHz rep rate, 3 mJ/pulse, 100 fs pulse width) with a Helios Ultrafast spectrometer used for detection. The fundamental beam was split into the pump and probe pulse directly after the Coherent laser. The pump laser was tuned with a Palitra Duo OPA to obtain varying excitation wavelengths needed for TR measurements. The probe beam was sent through a delay line before being transformed into a white light continuum using a Sapphire crystal. The pump and probe pulses were aligned on the sample, with the probe

pulse at a 45° angle to the sample. All samples were measured under ambient conditions. The excitation density for each wavelength was kept so that N_0 was approximately 4×10^{17} charge carriers/cm³.

Time resolved photoluminescence:

A Hamamatsu C10910-04 streak camera was used for detection and an NKT supercontinuum fiber laser (SuperK EXU-6-PP) for excitation. Samples were excited with 600 nm light.

Profilometry:

A Dektak 8 Advanced Development Profilometer was used to obtain sample thickness information. At least 3 scans were performed on each film and averaged to find the film thickness.

XRD:

X-ray diffraction patterns were measured with a Bruker D8 diffractometer equipped with a Hi-Star 2D area detector and a Cu K α radiation source. Scherrer analysis was performed by fitting peaks to a Lorentzian profile.

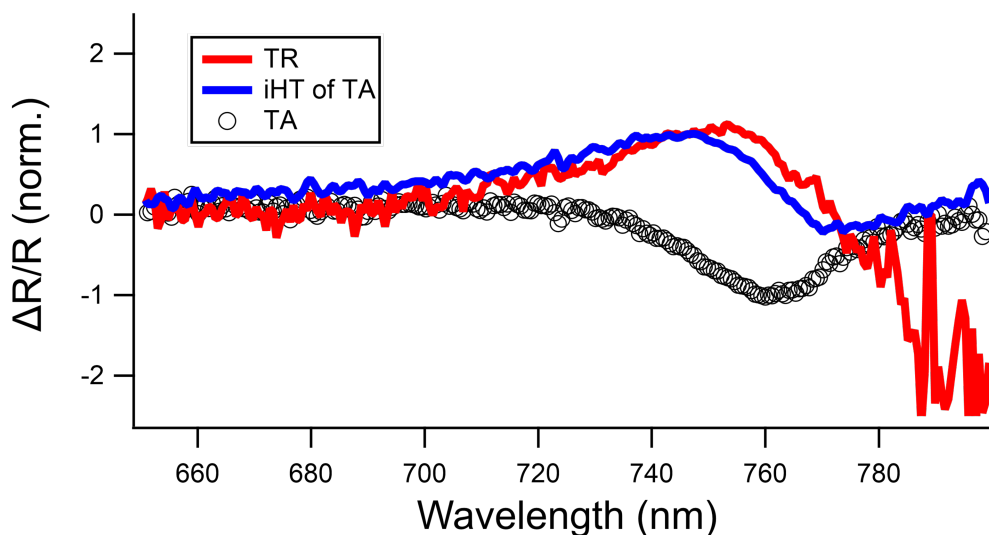


Figure S2: Transient absorption (grey circles), transient reflectance (red trace), and the inverse Hilbert transform of the transient absorption spectrum (blue trace). The TA signal shows a ground state bleach around 760 nm, typical of MAPI. Using the Kramers-Kronig relation, the transient absorption spectrum (grey) can be transformed into a simulation of the transient reflectance spectrum (blue). At wavelengths smaller than 750 nm (higher energy), the transform of the TA (blue) matches exactly with the transient reflectance spectrum (red). This indicates that at wavelength where the inverse Hilbert transform of the TA matches the TR, only changes in reflectance at the front (surface) of the sample is probed. Below 760 nm, an interference regime where signal from both the front and back surfaces of the perovskite is probed. This indicates that the kinetics for analysis should be taken from higher than 760 nm.

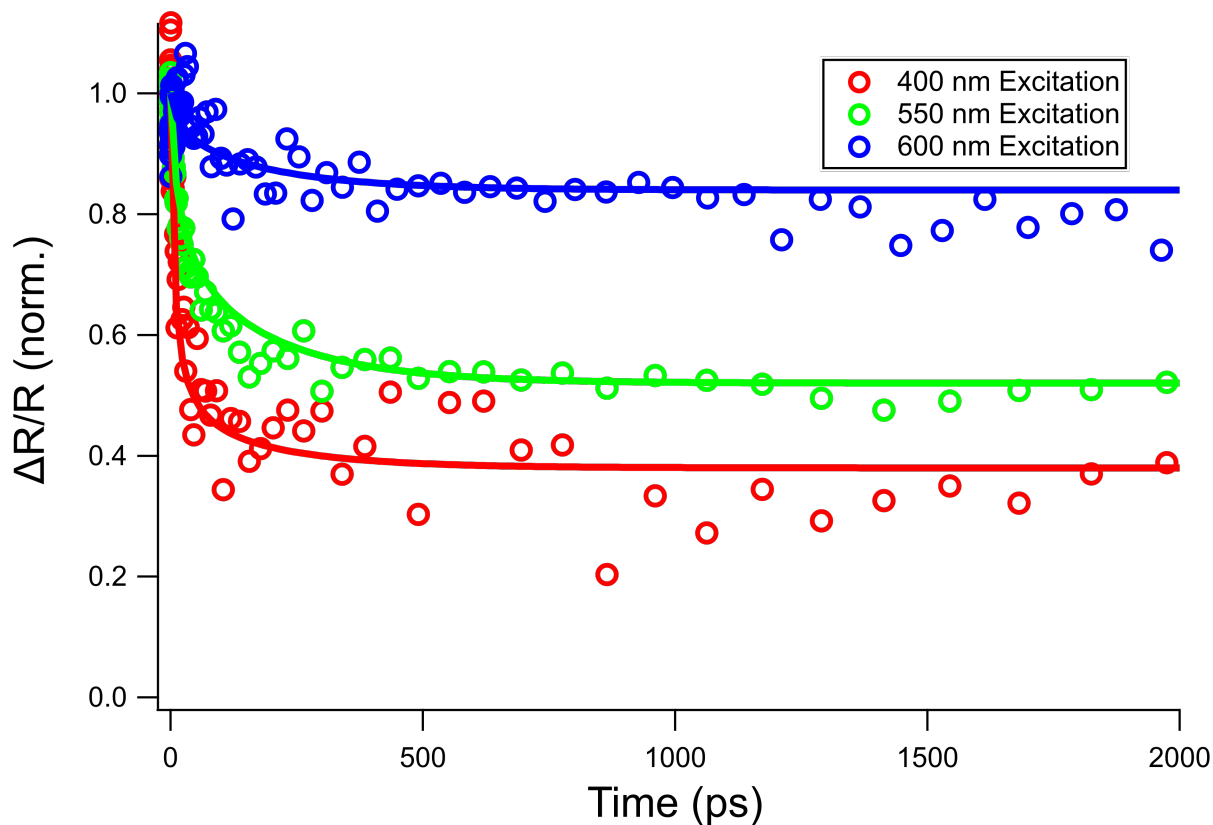


Figure S3: Transient reflectance kinetics (taken at 700 nm) for the 10% excess sample pumped at different wavelengths. Since the absorption coefficient of MAPI increases with increasing pump energies, lower energy pumps are able to excite farther into the film compared to high energy pumps. This allows for larger volumes of the film, and therefore more bulk-like (vs. surface) behavior, with decreasing pump energy. The higher the pump energy, the shorter the kinetic lifetime. Since the change in the signal across all three wavelengths is primarily concentrated to the first few hundred ps, then diffusion can be identified as the mechanism that contributes to the change in signal. Therefore, diffusion dominates at the surface. This data can be fit to a global analysis that can quantitatively extract the diffusion coefficient.¹⁸ The fitting procedure was performed on raw data without normalization. The 10% excess sample is representative for the data for 0, 2.5, and 5% excess as well.

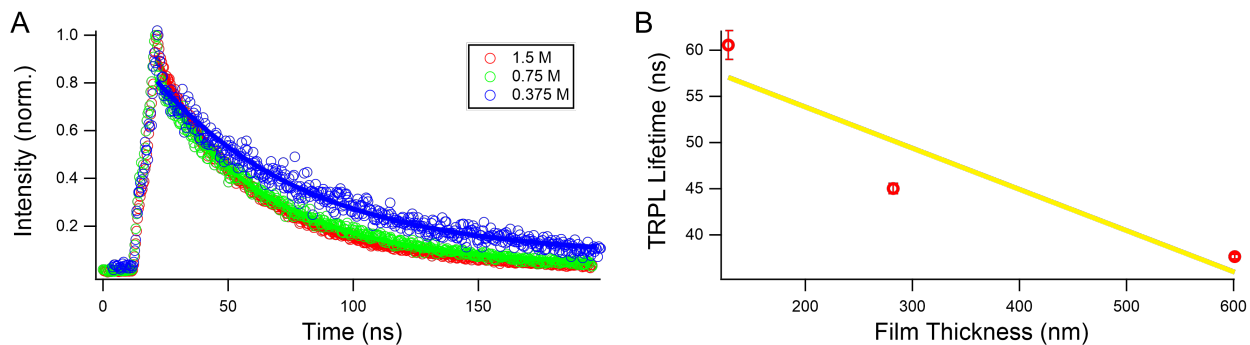


Figure S4: (A) Time resolved photoluminescence of 0% excess films. Films were made with precursors with varying molarity, which yields films with different thicknesses (as measured by profilometry, B). The films were excited with 600 nm light and the PL lifetime was then fit to a monoexponential decay. (B) The extracted lifetimes were then plotted against the film thickness so that a linear fit between TRPL lifetime and film thickness could be found. The inverse of this relationship yields the surface recombination lifetime in m/s. These results are reported in Fig. 4 of the main text.

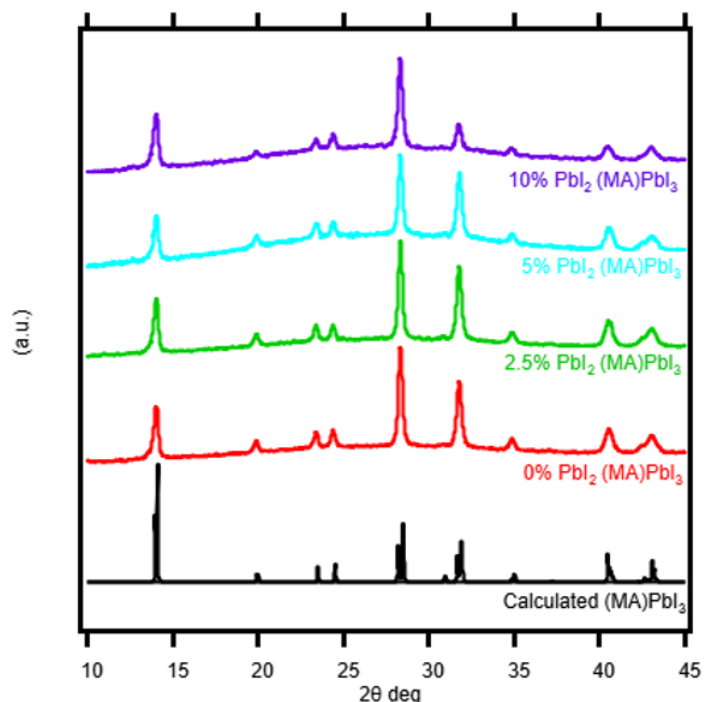


Figure S5: X-ray diffraction (XRD) patterns of freshly prepared MAPI thin films with varying PbI_2 content. The XRD patterns match well to the calculated MAPI pattern¹⁹ and are absent of any impurity peaks. The average crystallite size calculated from the Scherrer equation is 56 nm, 56 nm, 51 nm, 52 nm for 0%, 2.5%, 5%, 10% PbI_2 , respectively, indicating there is little variation with perovskite grain size with varying ratios of PbI_2 in the precursor.

References

- (1) Giannozzi, P. et al. QUANTUM ESPRESSO: a modular and open-source software project for quantum simulations of materials. *J. Phys.: Condens. Matter* **2009**, *21*, 395502.
- (2) Giannozzi, P. et al. Advanced capabilities for materials modelling with Quantum ESPRESSO. *J. Phys.: Condens. Matter* **2017**, *29*, 465901.
- (3) Perdew, J. P.; Burke, K.; Ernzerhof, M. Generalized Gradient Approximation Made Simple. *Phys. Rev. Lett.* **1996**, *77*, 3865–3868.
- (4) Heyd, J.; Scuseria, G. E.; Ernzerhof, M. Hybrid functionals based on a screened Coulomb potential. *J. Chem. Phys.* **2003**, *118*, 8207–8215.
- (5) Grimme, S.; Antony, J.; Ehrlich, S.; Krieg, H. A consistent and accurate ab initio parametrization of density functional dispersion correction (DFT-D) for the 94 elements H-Pu. *J. Chem. Phys.* **2010**, *132*, 154104.
- (6) Garrity, K. F.; Bennett, J. W.; Rabe, K. M.; Vanderbilt, D. Pseudopotentials for high-throughput DFT calculations. *Comput. Mater. Sci.* **2014**, *81*, 446–452.
- (7) Schlipf, M.; Gygi, F. Optimization algorithm for the generation of ONCV pseudopotentials. *Comput. Phys. Commun.* **2015**, *196*, 36–44.
- (8) Du, M.-H. Density Functional Calculations of Native Defects in CH₃NH₃PbI₃: Effects of Spin–Orbit Coupling and Self-Interaction Error. *J. Phys. Chem. Lett.* **2015**, *6*, 1461–1466.
- (9) Supasai, T.; Rujisamphan, N.; Ullrich, K.; Chemseddine, A.; Dittrich, T. Formation of a Passivating CH₃NH₃PbI₃/PbI₂ Interface during Moderate Heating of CH₃NH₃PbI₃ Layers. *Appl. Phys. Lett.* **2013**, *103*, 183906.

- (10) Ong, S. P.; Richards, W. D.; Jain, A.; Hautier, G.; Kocher, M.; Cholia, S.; Gunter, D.; Chevrier, V. L.; Persson, K. A.; Ceder, G. Python Materials Genomics (pymatgen): A robust, open-source python library for materials analysis. *Comput. Mater. Sci.* **2013**, *68*, 314 – 319.
- (11) Larsen, A. H. et al. The atomic simulation environment—a Python library for working with atoms. *J. Phys.: Condens. Matter* **2017**, *29*, 273002.
- (12) Momma, K.; Izumi, F. VESTA 3 for three-dimensional visualization of crystal, volumetric and morphology data. *J. Appl. Crystallogr.* **2011**, *44*, 1272–1276.
- (13) Meggiolaro, D.; De Angelis, F. First-Principles Modeling of Defects in Lead Halide Perovskites: Best Practices and Open Issues. *ACS Energy Lett.* **2018**, *3*, 2206–2222.
- (14) Stoumpos, C. C.; Malliakas, C. D.; Kanatzidis, M. G. Semiconducting Tin and Lead Iodide Perovskites with Organic Cations: Phase Transitions, High Mobilities, and Near-Infrared Photoluminescent Properties. *Inorg. Chem.* **2013**, *52*, 9019–9038.
- (15) Wyckoff, R. W. G. Crystal structures, 2nd edition. *Acta Crystallogr.* **1963**, *1*, 239–444.
- (16) Gražulis, S.; Chateigner, D.; Downs, R. T.; Yokochi, A. F. T.; Quirós, M.; Lutterotti, L.; Manakova, E.; Butkus, J.; Moeck, P.; Bail, A. L. Crystallography Open Database – an open-access collection of crystal structures. *J. Appl. Cryst.* **2009**, *42*, 726–729.
- (17) Elmelund, T.; Scheidt, R. A.; Seger, B.; Kamat, P. V. Bidirectional Halide Ion Exchange in Paired Lead Halide Perovskite Films with Thermal Activation. *ACS Energy Lett.* **2019**, *4*, 1961–1969.
- (18) Zhai, Y.; Wang, K.; Zhang, F.; Xiao, C.; Rose, A. H.; Zhu, K.; Beard, M. C. Individual Electron and Hole Mobilities in Lead-Halide Perovskites Revealed by Noncontact Methods. *ACS Energy Lett.* **2020**, *5*, 47–55.

- (19) Szafranski, M.; Katrusiak, A. Mechanism of Pressure-Induced Phase Transitions, Amorphization, and Absorption-Edge Shift in Photovoltaic Methylammonium Lead Iodide. *J. Phys. Chem. Lett.* **2016**, *7*, 3458–3466, PMID: 27538989.

Graphical TOC Entry

